

# Automated computation of nerve fibre inclinations from 3D polarised light imaging measurements of brain tissue

Miriam Menzel<sup>1,+,\*</sup>, Jan A. Reuter<sup>1,+</sup>, David Gräbel<sup>1</sup>, Irene Costantini<sup>2,3,4</sup>, Katrin Amunts<sup>1,5</sup>, and Markus Axer<sup>1</sup>

<sup>1</sup>Institute of Neuroscience and Medicine (INM-1), Forschungszentrum Jülich GmbH, Jülich, Germany

<sup>2</sup>European Laboratory for Non-Linear Spectroscopy, University of Florence, Florence, Italy

<sup>3</sup>Department of Biology, University of Florence, Florence, Italy

<sup>4</sup>National Institute of Optics, National Research Council, Rome, Italy

<sup>5</sup>Cécile and Oskar Vogt Institute for Brain Research, University Hospital Düsseldorf, Heinrich Heine University of Düsseldorf, Düsseldorf, Germany

\*Correspondence: m.menzel@fz-juelich.de

+these authors contributed equally to this work

## ABSTRACT

The method 3D polarised light imaging (3D-PLI) measures the birefringence of histological brain sections to determine the spatial course of nerve fibres (myelinated axons). While the in-plane fibre directions can be determined with high accuracy, the computation of the out-of-plane fibre inclinations is more challenging because they are derived from the strength of the birefringence signals (retardation), which depends e. g. on the amount of nerve fibres. One possibility to improve the accuracy is to consider the average transmitted light intensity (transmittance weighting). The current procedure requires effortful manual adjustment of parameters and anatomical knowledge. Here, we introduce an automated, optimised computation of the fibre inclinations, allowing for a much faster, reproducible determination of fibre orientations in 3D-PLI. Depending on the degree of myelination, the algorithm uses different models (transmittance-weighted, unweighted, or a linear combination), allowing to go beyond traditional definitions of white and grey matter and account for regionally specific behaviour. As the algorithm is parallelised and GPU optimised, and uses images from standard 3D-PLI (retardation and transmittance), it can be applied to large data sets, also from previous measurements. The functionality is demonstrated on unstained coronal and sagittal histological sections of vervet monkey and rat brains.

## Introduction

To better understand the brain's function and treat neurological diseases, a detailed reconstruction of the intricate and densely grown nerve fibre network is needed. The method *3D polarised light imaging* (3D-PLI) has been developed a decade ago to analyse the three-dimensional course of nerve fibre pathways in brain tissue with micrometer resolution<sup>1,2</sup>. The spatial nerve fibre orientations are derived by transmitting linearly polarised light through unstained histological brain sections and measuring the birefringence (optical anisotropy) for different directions of polarisation with a circular analyser. The phase of the measured birefringence signal is related to the in-plane orientation angle of the nerve fibres within the brain section (*direction*). The normalised amplitude of the signal (*retardation*) is related to the out-of-plane orientation angle of the nerve fibres (*inclination*). The birefringence signal is mainly caused by the myelin sheaths which surround most axons in the white matter<sup>3</sup>. In the following, the term *nerve fibre* will solely be used to refer to myelinated axons.

The in-plane direction angles of the nerve fibres can be determined with high degree of accuracy (provided the fibre bundles have a well-defined orientation and low to intermediate inclination<sup>4</sup>). The computation of the out-of-plane inclination angles requires a more sophisticated analysis: In principle, the fibre inclination  $\alpha$  is related to the retardation  $r$  (strength of birefringence) via<sup>5</sup>:  $r \propto \cos^2 \alpha$ . However, the retardation also depends on other factors such as the amount of nerve fibres, which varies between image pixels<sup>6</sup>. In order to determine the out-of-plane fibre inclinations independent of the tissue composition, a tiltable specimen stage can be used<sup>7</sup>: By repeating the 3D-PLI measurement for different tilting angles, it is possible to change the perspective onto the nerve fibres in a predictable manner and reconstruct the fibre inclinations. However, most high-resolution polarising microscopes are not equipped with a tilting stage. An alternative way to adjust the determined inclination angles is to use the transmittance (polarisation-independent transmitted light intensity) as a measure of the amount



of nerve fibres in the brain section (*transmittance weighting*)<sup>8</sup>: Due to its highly layered structure, myelin has a large scattering coefficient<sup>9</sup> so that regions with a high density of nerve fibres (myelinated axons) appear dark in the transmittance.

Previous work of our group<sup>10</sup> has shown that the transmittance is not solely a measure of the myelin density, but also depends on the inclination of the nerve fibres: regions with out-of-plane nerve fibres show a lower transmittance than in-plane nerve fibres, even if they contain the same amount of nerve fibres.

In addition, the transmittance can only serve as a measure of the myelin density (amount of nerve fibres) if the attenuation of myelin is dominant compared to the attenuation of other tissue components. Apart from myelinated axons, brain tissue contains unmyelinated axons, neuronal cell bodies, dendrites, synapses, glial cells, and blood capillaries, which are all differently distributed and have locally variable attenuation properties. Therefore, in regions with a low amount of myelinated axons, the transmittance cannot serve as a measure of myelination. Morphologically, brain tissue can be divided into white matter (containing a larger amount of nerve fibres) and grey matter (containing a larger amount of cell bodies and other tissue components)<sup>3,11</sup>. However, as white and grey matter are not easily distinguishable without expert knowledge and the optical properties depend on the very tissue composition, they cannot be used to identify suitable regions for transmittance weighting. Instead, the degree of myelination should be considered, as it determines if the transmittance is dominated by the scattering of myelin (nerve fibres).

Up to now, the nerve fibre inclinations were computed using a transmittance-weighted model for the whole brain section, requiring manual adjustment of the resulting parameters and advanced anatomical knowledge to account for different tissue compositions. Based on transmittance and retardation histograms, an expert needed to iteratively adjust various threshold parameters to identify the optimum set of parameters that yields particular fibre inclinations in anatomically known brain regions while reducing the number of saturated regions with under/over-estimated fibre inclinations ( $\alpha = 0^\circ$  or  $90^\circ$ ).

Here, we introduce a fully automated computation of the nerve fibre inclinations, taking the inclination-dependence of the transmittance and different degrees of myelination into account. Instead of applying the transmittance-weighted model to the whole brain section, we use a regionally specific computation of fibre inclinations: The transmittance-weighted model is only used in regions with a high degree of myelination. In regions with a low degree of myelination, an unweighted model is used. The separation of regions with low and high degrees of myelination is based on an algorithm proposed by Benning *et al.*<sup>12</sup>. However, instead of using a binary classification, we introduce the important concept of transition zones, allowing to consider subtle changes in the tissue composition and to compute more accurate fibre inclinations at boundaries. As the automated computation does not require any manual adjustment of parameters, it allows for a much faster and reproducible computation of the three-dimensional nerve fibre orientations for 3D-PLI measurements of brain tissue.

## Results

To account for regions with different amounts of nerve fibres (myelinated axons), the transmittance was included in the computation of fibre inclinations because it is impaired by strong scattering of myelin. Depending on the degree of myelination (amount of nerve fibres), different models were used to compute the fibre inclinations: In regions with low myelination (*LM-regions*), the transmittance cannot serve as a measure of the amount of myelin because it is dominated by the attenuation of other tissue components such as cell bodies. Therefore, the fibre inclinations in LM-regions ( $\alpha_{LM}$ ) were computed with an *unweighted model* that is solely based on the measured birefringence (retardation value  $r \propto \cos^2 \alpha$ ) and uses the maximum retardation in LM-regions ( $r_{\max,LM}$ ) as reference:

$$\alpha_{LM} = \arccos \left( \sqrt{\frac{\arcsin(r)}{\arcsin(r_{\max,LM})}} \right). \quad (1)$$

In regions where the attenuation is mainly caused by the scattering of myelin, i. e. regions with high myelination (*HM-regions*), the transmittance ( $I_T$ ) can serve as a measure of the amount of myelin (nerve fibres). In these regions, the fibre inclinations ( $\alpha_{HM}$ ) were computed by means of a *transmittance-weighted model*, taking the extreme values of the transmittance in the regions with minimum and maximum myelin density ( $I_c$  and  $I_M$ ) into account (see Methods for more details):

$$\alpha_{HM} = \arccos \left( \sqrt{\frac{\arcsin(r)}{\arcsin(r_{\max,HM})} \cdot \frac{\ln(I_c/I_M)}{\ln(I_c/I_T)}} \right). \quad (2)$$

In transition zones between LM- and HM-regions, a linear combination of both models was used:

$$\alpha = (P_{HM} - 1) \cdot \alpha_{LM} + P_{HM} \cdot \alpha_{HM}, \quad (3)$$

where  $P_{HM} \in [0, 1]$  denotes the probability that a region is highly myelinated (HM).



## Determination of the degree of myelination

To start with, we used the binary classification by Benning *et al.*<sup>12</sup> to separate regions with low and high myelination (LM- and HM-regions). Note that we here use the terms LM- and HM-regions (and not “grey matter” and “white matter” as Benning *et al.*) to avoid confusion with the anatomical definitions. The separation of regions was performed by calculating three threshold parameters ( $r_{\text{thres}}$ ,  $I_{\text{thres}}$ ,  $I_{\text{back}}$ ) from the histograms of the retardation ( $r$ ) and transmittance ( $I_T$ ) images, see Methods for more details: While all regions with high birefringence ( $r > r_{\text{thres}}$ ) can be considered as HM-regions, not all regions with low birefringence ( $r \leq r_{\text{thres}}$ ) can be considered as LM-regions because regions with crossing fibres, out-of-plane fibres, or a smaller number of nerve fibres also result in smaller birefringence values. As in-plane crossing and out-of-plane fibres have similar or even lower transmittance values than regions with in-plane fibres<sup>10</sup>, the transmittance in a region with many in-plane fibres, i. e. maximum retardation ( $I_{\text{rmax}}$ ), can be used as reference: Hence, HM-regions are defined by regions with similar or lower transmittance values ( $I_T \lesssim I_{\text{rmax}}$ ), while LM-regions are restricted to regions with higher transmittance values ( $I_T > I_{\text{rmax}}$ ), and background (not containing any tissue) to regions with much higher transmittance values ( $I_T \gg I_{\text{rmax}}$ ). For better separation,  $I_{\text{thres}}$  and  $I_{\text{back}}$  were used as threshold parameters (see Fig. 1a). The threshold parameters  $r_{\text{thres}}$ ,  $I_{\text{thres}}$ , and  $I_{\text{back}}$  correspond to points of maximum curvature in the histograms (see Methods).

- HM-regions (high myelination):  $(r > r_{\text{thres}}) \vee (I_T < I_{\text{thres}})$ ,
- LM-regions (low myelination):  $(r \leq r_{\text{thres}}) \wedge (I_{\text{thres}} \leq I_T \leq I_{\text{back}})$ ,
- Background (no tissue):  $I_T > I_{\text{back}}$ .

When computing the inclination angles for HM- and LM-regions separately, we obtain artificially sharp borders, e. g. in regions where nerve fibres from the white matter spread out into the cortex. To account for regions that do not clearly belong to one or the other tissue type, transition zones between HM- and LM-regions were identified. To determine the width of the transition zones, the threshold parameters  $r_{\text{thres}}$  and  $I_{\text{thres}}$  were considered, which have a major impact on the separation of HM- and LM-regions (cf. striped areas in Fig. 1a): In a transition zone, slight changes of the threshold parameters cause the region to be identified as a different tissue type. To find out whether a separation is susceptible to small changes, the threshold parameters were recomputed several times from slightly different retardation and transmittance histograms that were generated by bootstrapping (random sampling with replacement): Pixels were randomly drawn from the retardation and transmittance images, and the same pixel could be selected multiple times. To identify the best compromise between computing time and accuracy, the algorithm was run for different sample sizes (100 %, 25 %, 4 %, 1 % of all image pixels) for 500 iterations. From

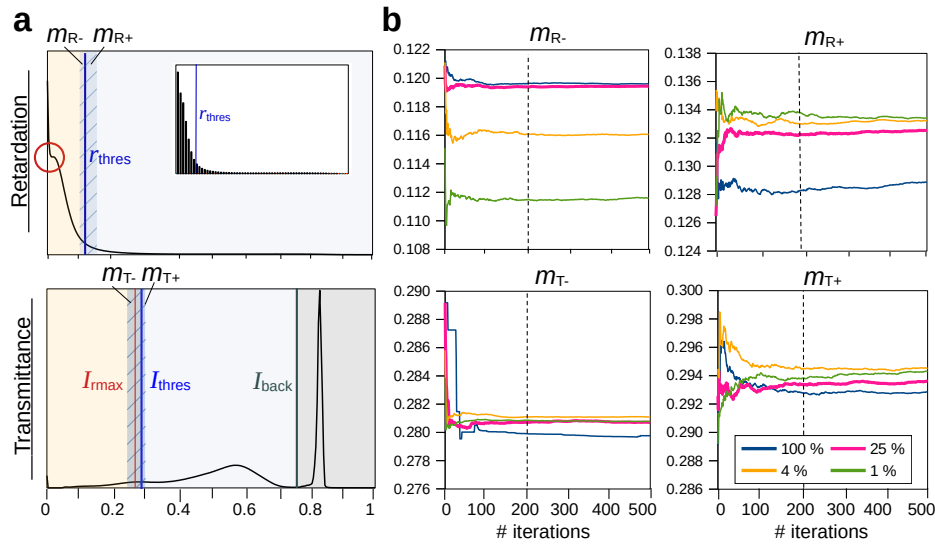


**Figure 1.** Optimum choice of iteration number and sample size when computing the HM-probability map, shown exemplary for a coronal rat brain section (cf. Fig. 6b). (a) Corresponding retardation and transmittance histograms (256 bins). The parameters  $r_{\text{thres}}$ ,  $I_{\text{rmax}}$ ,  $I_{\text{thres}}$ , and  $I_{\text{back}}$  are indicated by vertical solid lines. When computing the histograms from different sets of image pixels, the threshold parameters  $r_{\text{thres}}$  and  $I_{\text{thres}}$  may vary (indicated by striped areas). The corresponding positive/negative means are denoted by  $m_{R+/-}$  and  $m_{T+/-}$ , respectively. The inset in the retardation histogram shows the histogram with 64 bins, used to determine the correct position of the threshold parameters (see Methods for more details). (b) Positive and negative means of  $r_{\text{thres}}$  and  $I_{\text{thres}}$ , computed for up to 500 iterations and different sample sizes (100 %, 25 %, 4 %, 1 % of all image pixels).



the resulting values for  $r_{\text{thres}}$  and  $I_{\text{thres}}$ , the *positive/negative means* ( $m_{R+/-}$  and  $m_{T+/-}$ ) were computed, respectively, i. e. the mean of all values that are larger/smaller than the original value. This whole process was repeated 10 times and the average values for each iteration were forwarded to further analysis.

Figure 1b shows the positive and negative means for the different sample sizes and up to 500 iterations for a coronal rat brain section (shown in Fig. 6b). The different sample sizes yield similar curves. The smaller the sample size, the more the values differ from the ones obtained with 100 % sample size. After 200 iterations (vertical dashed line), the values for 100 % and 25 % sample size (blue and magenta curves) do not change much and the maximum difference between 25 % and 100 % sample size is still within one histogram bin ( $1/256 = 0.0039$ ). Therefore, a sample size of 25 % and 200 iterations were selected for computing  $m_{R+/-}$  and  $m_{T+/-}$ .

The  $m$ -values were used to define the width of the transition zone which was described by a trigonometric error function (see Methods and top image of Fig. 2c). The result is an *HM-probability map* which indicates the probability  $P_{\text{HM}}$  that a region is highly myelinated (HM-region): regions with  $P_{\text{HM}} > 0.95$  were considered as HM-regions, regions with  $P_{\text{HM}} < 0.05$  as LM-regions, and everything in between as transition zone. Figure 2a shows the HM-probability map of a coronal vervet monkey brain section (HM-regions in white, LM-regions in black, transition zone in different colours).

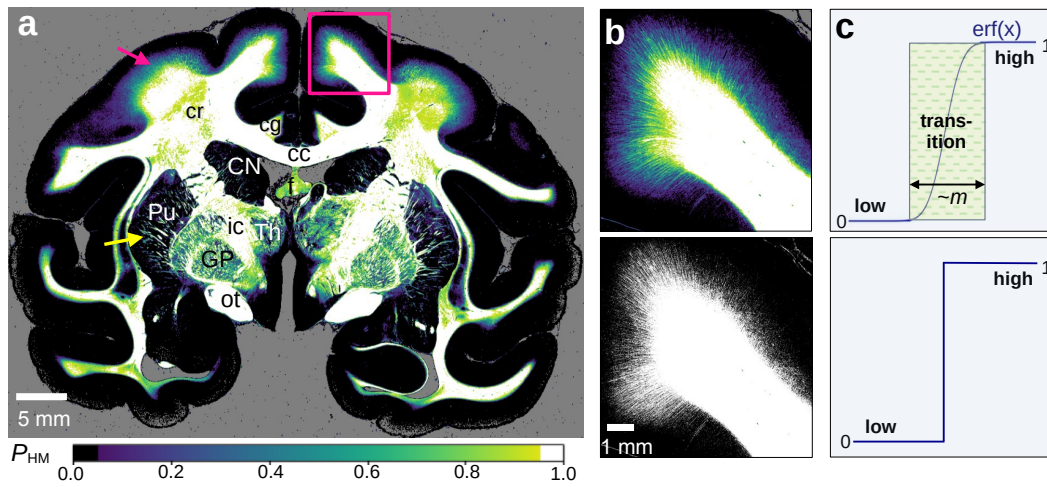


**Figure 2.** Myelination maps of a coronal vervet brain section. (a) HM-probability map of the whole section (computed with 25 % sample size and 200 iterations). Regions with  $P_{\text{HM}} < 0.05$  are considered to have low myelination (LM-regions, in black), regions with  $P_{\text{HM}} > 0.95$  are considered to have high myelination (HM-regions, in white). The transition zone is shown in different colours. The magenta and yellow arrow point to regions with a smooth and sharp transition, respectively. cc = corpus callosum, cg = cingulum, cr = corona radiata, f = fornix, ic = internal capsule, ot = optic tract, CN = caudate nucleus, GP = globus pallidus, Pu = putamen, Th = thalamus. (b) Enlarged view of the region marked by the magenta rectangle in (a). The top image shows the HM-probability map, the bottom image shows a sharp separation between HM/LM-regions without any transition zone. (c) Sketch of the functions used to describe the transition zone between HM/LM-regions. In the HM-probability map, an error function  $\text{erf}(x)$  is used to describe the transition zone (top), the width depends on the computed mean  $m$  of the threshold parameters, cf. Fig. 1b. The bottom figure illustrates the binary classification. LM = 0, HM = 1.

While there is a sharp separation between fibre bundles and surrounding tissue in the putamen (yellow arrow), there is a smooth transition for fibres spreading from the white matter into the cortex (magenta arrow). The slightly lower  $P_{\text{HM}}$ -values in the corona radiata (cr), which is a region rich of white matter tracts, are due to the steep and crossing nerve fibres which impair the classification of regions (see Discussion).

### Correction of transmittance values

As the transmittance is used to correct the fibre inclinations in the HM-regions (cf. equation 2), cellular structures in the transmittance image might lead to artifacts in the resulting inclination image. Therefore, a blurred transmittance was employed to compute the inclination, applying a median filter with circular kernel. Figure 3a shows the median-filtered transmittance image of the coronal vervet brain section with a kernel radius of five pixels. Figure 3c shows an enlarged view of the region covered by the red rectangle for a kernel radius of two pixels (top) and seven pixels (bottom). For a kernel size of two pixels, fine structural details are still visible, especially in the cortex. When using a larger kernel size of 7 pixels, the structures become blurry and lead to clouding artefacts in the resulting inclination image. We therefore selected a kernel radius of 5 pixels as



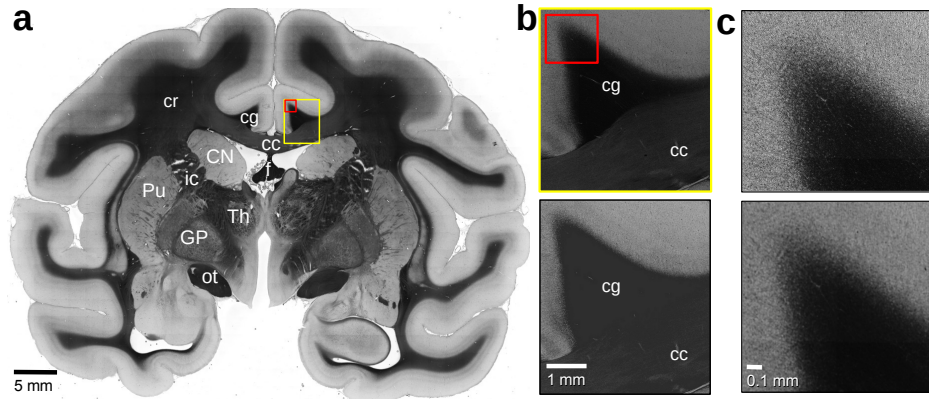


**Figure 3.** Correction of transmittance values. (a) Median-filtered transmittance image of the coronal vervet brain section (circular kernel with 5 px radius). Anatomical regions are labelled for better reference (refer to Fig. 2). (b) Comparison of transmittance images (median-filtered with 5 px radius for the region covered by the yellow rectangle) before (top) and after (bottom) shifting the transmittance values of out-of-plane nerve fibres to  $I_{\text{rmax}}$ . (c) Comparison of different median filter sizes for the region covered by the red rectangle: kernel radius of 2 pixels (top) and 7 pixels (bottom).

best compromise. To retain sharp borders between HM- and LM-regions, the median filter was applied to HM- and LM-regions exclusively.

Before using the transmittance to compute the inclination, another correction was applied: As mentioned in the Introduction, the transmittance for out-of-plane nerve fibres is lower than for in-plane nerve fibres due to an increase of scattering. This leads to an over-estimation of transmittance-weighted inclinations (the model assumes that the transmittance depends only on the amount of nerve fibres and not on their inclination). To overcome this problem, the transmittance of the region with maximum retardation ( $I_{\text{rmax}}$ ), which is expected to lead to the highest degree of absorption, was used as reference. All regions with lower transmittance values were clipped to the minimum transmittance  $I_{\text{rmax}}$  in areas where  $I_{\text{T}} \leq I_{\text{rmax}}$ . Figure 3b shows the median-filtered transmittance image (enlarged view of the region marked by the yellow rectangle) without correction (top) and with correction (bottom). Without correction, the transmittance values of the cingulum (cg), which contains mostly very steep out-of-plane fibres, are notably darker than those of the corpus callosum (cc), which contains mostly in-plane fibres. The same applies to the fornix (f) and the optic tract (ot).

### Computation of nerve fibre inclinations

After identifying the HM- and LM-regions and their transition zones (HM-probability map), the retardation and corrected transmittance images were used to compute the fibre inclination angles, taking the respective value of the HM-probability map into account (see Methods).

### Comparison of different models

To illustrate the difference between the unweighted model and the transmittance-weighted model for computing the fibre inclination (equations 1 and 2) as well as the effect of the transition zone between HM- and LM-regions (equation 3), the fibre inclinations were computed for different models (see Fig. 4): (i) unweighted model ( $\alpha_{\text{LM}}$ ) applied to whole brain section, (ii) transmittance-weighted model ( $\alpha_{\text{HM}}$ ) applied to whole brain section, (iii) unweighted and transmittance-weighted models applied to LM- and HM-regions separately, and (iv) unweighted and transmittance-weighted models applied to LM- and HM-regions using the HM-probability map combining both formulas in the transition zone.

When applying the unweighted model to the whole image, using the maximum retardation of the brain section as reference ( $r_{\text{max,LM}} = r_{\text{max}}$ ), the fibre inclinations in the grey matter are highly over-estimated (Fig. 4(i)). On the other hand, when applying the transmittance-weighted model to the whole image ( $r_{\text{max,HM}} = r_{\text{max}}$ ), the fibre inclinations in the grey matter are under-estimated, generating a lot of saturated values at  $\alpha = 0^\circ$  in black (Fig. 4(ii)). When applying the two different models to HM- and LM-regions exclusively, using their maximum retardation as reference ( $r_{\text{max,HM}}$ ,  $r_{\text{max,LM}}$ ), the estimated fibre inclinations become more realistic throughout the entire brain section. The contrast between out-of-plane fibres (cingulum = cg) and in-plane fibres, both in regions with densely packed nerve fibres (corpus callosum = cc) and in regions with bulked fibre architecture (cortex), becomes clearly visible (Fig. 4(iii)). However, the sharp separation of HM- and LM-regions leads to an underestimation of the inclination (dark pixels) in regions where fibres extend to cortical areas (see yellow arrow in (III)), even worsening where sharp bending is involved (cyan arrows in (III)). The fourth model using the HM-probability map to combine the formulas for HM- and LM-regions in the transition zone reduces the underestimation considerably, leading to a



more continuous course of fibres from deep white matter regions into the cortex (see yellow and cyan arrows in (IV)).

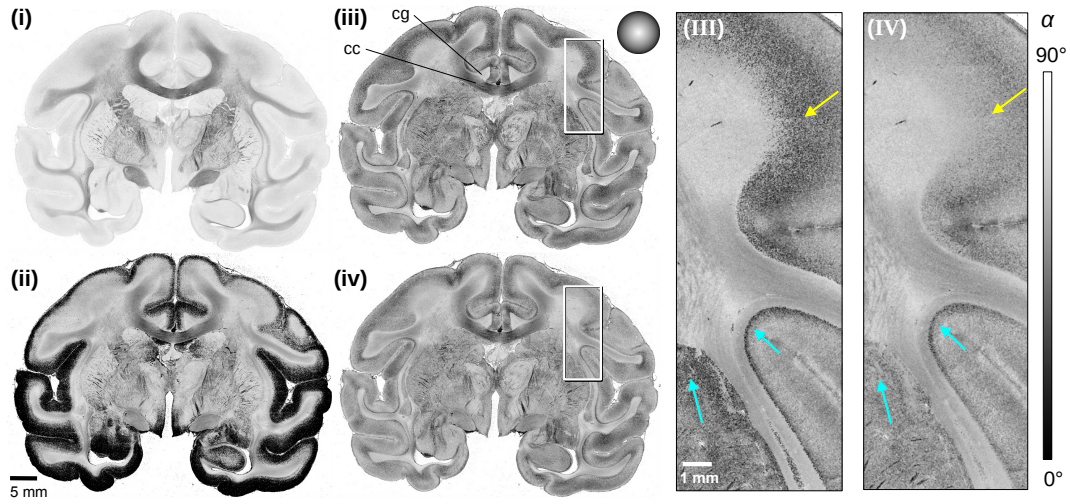


**Figure 4.** Inclination maps of the coronal vervet brain section computed with different models (equations 1 to 3): (i) unweighted model ( $\alpha_{LM}$ ) applied to whole section, (ii) transmittance-weighted model ( $\alpha_{HM}$ ) applied to whole section, (iii) both models applied separately to LM- and HM-regions, (iv) linear transition between both models depending on the computed HM-probability value. The images on the right ((iii) and (iv)) show enlarged views of the regions marked by the white rectangles in (iii) and (iv), respectively. cc = corpus callosum, cg = cingulum. The yellow and cyan arrowheads point to two different types of transition zones located between LM- and HM-regions.

#### Comparison to measurements acquired with two-photon fluorescence microscopy

To quantitatively evaluate the automatically computed nerve fibre inclinations, the caudate putamen of a coronal rat brain section was measured both with 3D-PLI and with *two-photon fluorescence microscopy* (TPFM)<sup>13–15</sup>, see Fig. 5a,b and Methods.

TPFM allows an in-depth scan of the sample and directly assesses the three-dimensional course of nerve fibre bundles in the caudate putamen (cf. Fig. 5c), so that it can serve as a comparison for the nerve fibre orientations determined by 3D-PLI. 230 fibre bundles with well-defined shape and orientation were selected for evaluation (Fig. 5a,b). The average 3D-PLI inclination of each bundle was plotted against the TPFM inclination, which was geometrically reconstructed from the corresponding bundle (see Methods for more details). Figure 5d,e show the results for the in-plane fibre direction angle  $\varphi$  and the out-of-plane fibre inclination angle  $\alpha$  for the four different scenarios displayed in Fig. 4.

While the direction angles computed from 3D-PLI correspond mostly to those obtained from TPFM (see Fig. 5d), the computed 3D-PLI inclination angles are generally larger than those obtained from TPFM (see Fig. 5e). When applying the unweighted model to the whole brain section (i), the computed 3D-PLI inclinations are highly over-estimated, especially for lower fibre inclinations ( $< 50^\circ$ ). The computed 3D-PLI inclinations range between  $50^\circ$  and  $70^\circ$ , mostly independent of the actual inclination of the nerve fibres. When applying the transmittance-weighted model to the whole brain section (ii), the computed 3D-PLI inclinations become much more similar to those obtained from TPFM. However, even when taking their standard deviations ( $\Delta\alpha \approx 30^\circ$ ) into account, most values do not reach the TPFM inclinations. When applying the unweighted and transmittance-weighted models separately to LM- and HM-regions (iii), a global shift of the 3D-PLI inclinations of about  $-5^\circ$  can be observed. When using a linear transition between the models (iv), the computed 3D-PLI inclinations are still over-estimated, but the difference to the fibre inclinations derived from the TPFM measurements becomes slightly smaller at higher inclinations.

#### Inclination of fibres in coronal and sagittal brain sections

Figure 6 shows the HM-probability maps and the corresponding inclination maps (computed from equation 3) for coronal and sagittal sections of vervet monkey and rat brains.

The HM-probability maps reliably separate regions with low myelination (black) from the rest. Individual nerve fibres are visible in the putamen (Pu) of the coronal vervet brain section, and in the caudate putamen (CPu) of the coronal and sagittal rat brain sections. The HM-probability values in the white matter are slightly reduced (light green) for in-plane crossing fibres (cr) and steep out-of-plane fibres (coronal: cg, f; sagittal: cc), yielding slightly lower estimations of the inclination angles (cf. Fig. 5e). The inclination maps show a good distinction of regions with in-plane and out-of-plane nerve fibres. Although the coronal and sagittal sections belong to different brains, the different section planes (coronal/sagittal) clearly show an inverse



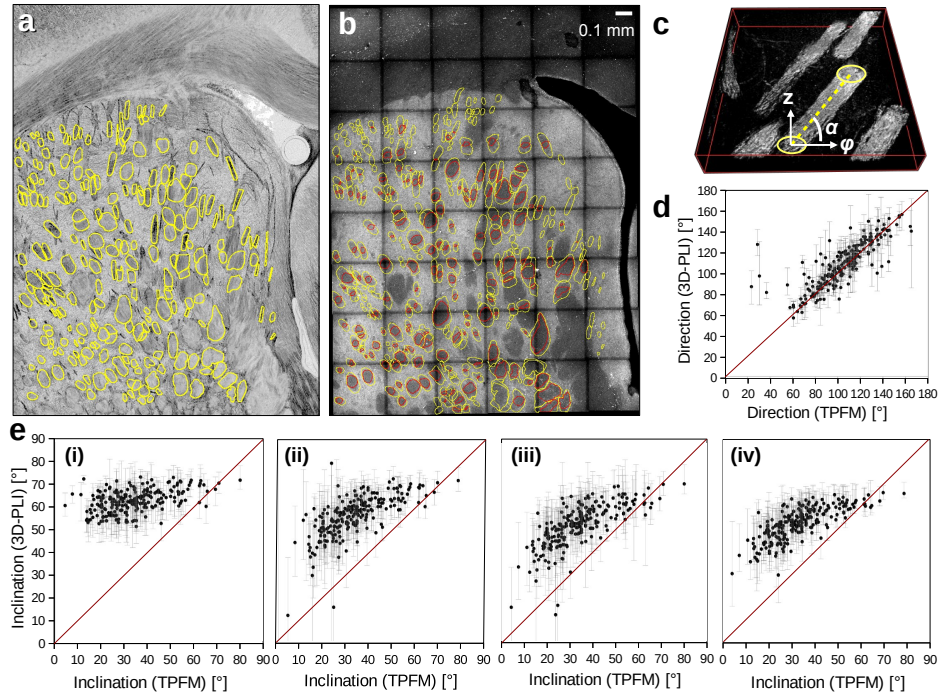


**Figure 5.** Comparison of 3D-PLI and TPFM nerve fibre orientations for a coronal rat brain section (230 selected fibre bundles in the caudate putamen). **(a)** Inclination map obtained from the 3D-PLI measurement (using equation 3). The fibre bundles selected for evaluation are labelled by yellow lines. **(b)** Maximum intensity projection of the TPFM image stack (containing  $6 \times 8$  tiles). The yellow contours show the first and the last fully visible cross-sections of the fibre bundles in the TPFM image stack which were used to geometrically reconstruct the fibre inclinations. The red shapes denote the overlap of the cross-sections. **(c)** Contrast-enhanced 3D-model of the TPFM image stack (1 tile, adapted from Menzel *et al.*<sup>10</sup>, Fig. S2c). The three-dimensional fibre orientation (dashed yellow line, defined by the in-plane direction angle  $\varphi$  and the out-of-plane inclination angle  $\alpha$ ) was geometrically computed from the centres of gravity of the bundle cross-sections mentioned above (yellow shapes). **(d)** Direction angles of the fibre bundles derived from the aligned 3D-PLI and TPFM measurements. The grey bars denote the positive and negative standard deviation when averaging the pixel values over the selected regions in the 3D-PLI direction image. **(e)** Inclination angles of the fibre bundles derived from the aligned 3D-PLI and TPFM measurements. The 3D-PLI inclinations were computed for four different scenarios (cf. Fig. 4): (i) unweighted model ( $\alpha_{LM}$ ) applied to whole brain section, (ii) transmittance-weighted model ( $\alpha_{HM}$ ) applied to whole brain section, (iii) unweighted and transmittance-weighted models applied to LM- and HM-regions separately, (iv) unweighted and transmittance-weighted models applied to LM- and HM-regions using a linear combination of both formulas in the transition zone.

pattern: In the coronal section plane, the computed inclination angles of the corpus callosum (cc) are much lower than those in the cingulum (cg) or the fornix (f). In the sagittal section plane, it is exactly the other way around.

## Discussion

When analysing measurement data from 3D-polarised light imaging (3D-PLI) of histological brain sections, the determination of the out-of-plane nerve fibre inclinations has been a major challenge, requiring anatomical knowledge and effortful manual adjustment of parameters. Here, we introduced an automatic computation of the fibre inclinations, by evaluating the retardation and transmittance images (normalised amplitude and average of the measured 3D-PLI signal). As these images are generated during standard 3D-PLI measurements, past measurements can be easily evaluated to improve the interpretation of fibre orientations in 3D-PLI data. In particular, no special equipment like a tilting stage is required to compute the nerve fibre inclinations. In contrast to the manual adjustment, no expert knowledge is required, the results for each measured brain section are reproducible, and large data sets can be analysed. In this way, we were able to provide a reliable estimate of the nerve fibre inclinations, which can still be adjusted by an expert in a second step.



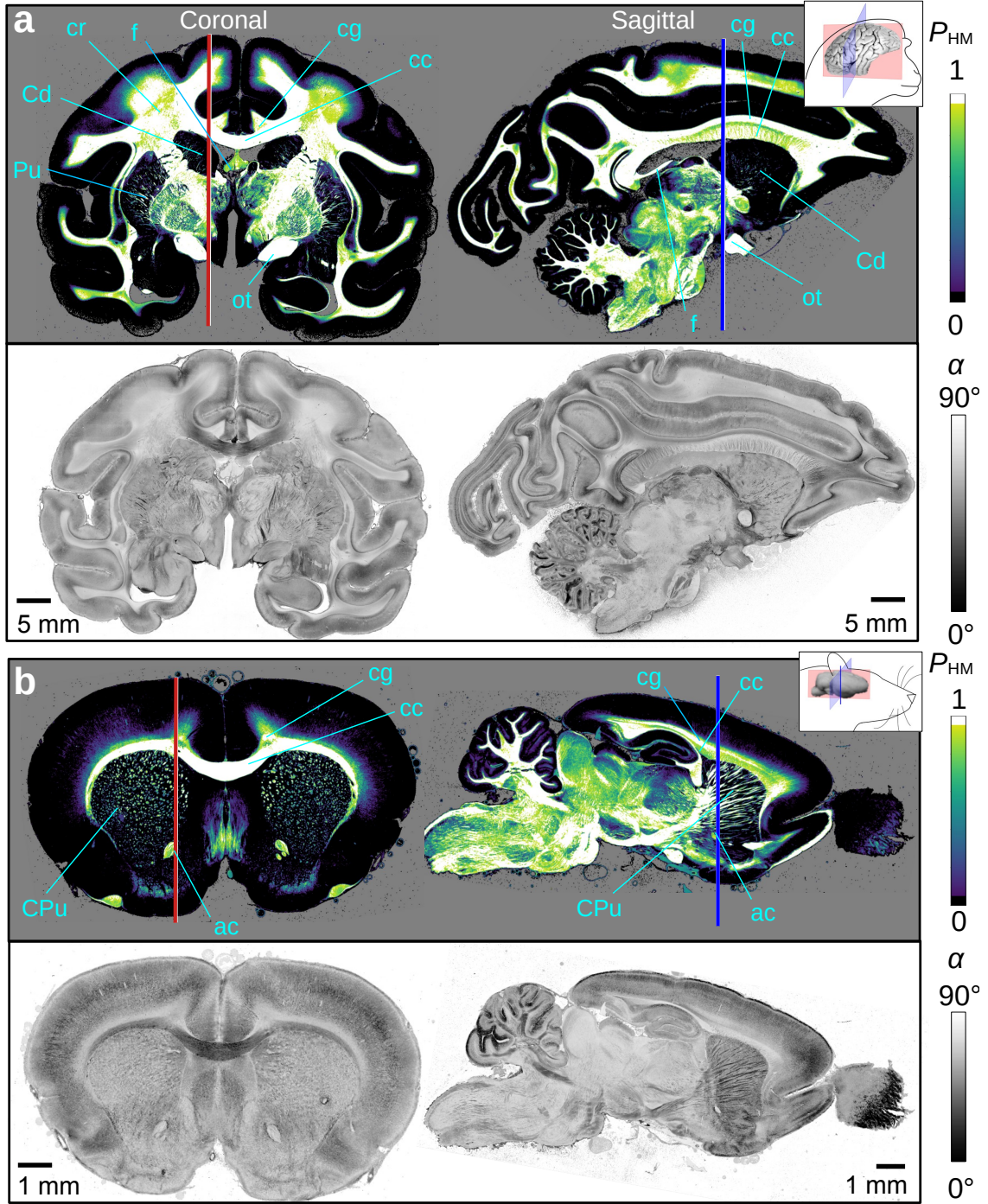


**Figure 6.** HM-probability and inclination maps of coronal and sagittal sections of vervet monkey brains (a) and rat brains (b). The upper images show the HM-probability maps  $P_{HM}$  computed from 200 iterations and 25 % sample size (see Methods for more details). The lower images show the inclination maps  $\alpha$  computed from the linearly combined formulas of LM- and HM-regions (equation 3), using the HM-probability value. The red and blue vertical lines indicate the approximate position of the sagittal and coronal section plane in the complementary brain section. Selected anatomical regions are labelled for reference (ac = anterior commissure, cc = corpus callosum, cg = cingulum, cr = corona radiata, f = fornix, ot = optic tract, Cd = caudate nucleus, CPu = caudate putamen, Pu = putamen).

In addition to the fibre inclinations, we provided an HM-probability map, indicating the probability that a region is highly myelinated. Benning *et al.*<sup>12</sup> proposed a binary separation of regions with low and high myelination. We improved the



existing algorithm (taking different features/plateaus of the histograms into account and excluding background tissue when determining the threshold parameters, see Methods). Furthermore, we introduced the important concept of transition zones. The classification of brain regions into regions with high myelination (HM-regions), low myelination (LM-regions), and transition zones is not only relevant when applying different inclination formulas. Another possible application might be Independent Component Analysis (ICA), which has been used for noise and artefact removal in 3D-PLI images<sup>16</sup>, especially in regions with low myelination (low birefringence signals)<sup>12</sup>. The HM-probability map allows to determine different degrees of myelination, helping to improve the ICA in those regions and enabling enhanced tissue segmentation.

The HM-probability maps and fibre inclinations were computed with a specifically developed open-source software, which is parallelised and uses GPU acceleration to efficiently process large images (see Methods for more details). While the computation of the fibre inclinations takes less than 5 min for the coronal vervet brain section ( $34\,669 \times 46\,341$  px), the generation of the HM-probability map takes about 15 min. The choice of the reduced sample size and number of iterations (cf. Fig. 1b) has therefore a large impact on the computing time. When using 100 % instead of 25 % sample size, four times more computing time (i. e. more than one hour) is required. To further reduce computing time, the number of iterations can be reduced to 100 without noticeable deviation of the threshold parameters from their asymptotic optimum (cf. Fig. 1b). Also, a more advanced bootstrapping approach (requiring smaller sample sizes) could be employed. The program could be extended to run on multiple GPUs, using the chunking algorithm that is already present. This would allow to process even larger brain sections and ideally achieve a linear speed-up.

While the software was shown to yield reliable results and correctly reproduce the overall inclination of major nerve fibre structures, several aspects should to be taken into account. First of all, the transmittance-weighted model used to compute the fibre inclinations in the HM-regions depends on the transmittance values. When the transmittance image has not enough contrast (e. g. in brain sections measured several days/weeks after tissue embedding) or when the transmittance image shows irregularities (caused e. g. by an inhomogeneous distribution of the embedding glycerine solution or tile/stitching artefacts), this leads to artefacts in the resulting inclination map, which would not be visible when solely using the birefringence signal (retardation) for computing the inclination (as in the LM-regions). Hence, the software should only be used when the transmittance image contrast is free of artefacts. Another point to take into account is that the algorithm uses the transmittance and retardation histograms to compute threshold parameters for the HM-probability map and other parameters in the inclination formulas. A reliable computation of parameters only works when the histograms include a broad variety of tissue components, both white and grey matter, as well as various nerve fibre structures (in-plane and out-of-plane fibres).

While the computed inclinations can serve as an estimate of the real out-of-plane angle in homogeneous nerve fibre tissue, they are highly over-estimated in regions with in-plane crossing nerve fibres due to the reduced birefringence signal<sup>6</sup>. As shown in Menzel *et al.*<sup>10</sup>, the transmittance image can serve as an indicator whether large inclination angles belong to out-of-plane nerve fibres or are caused by in-plane crossing fibres or a low fibre density. Regions with high inclination values can be considered as reliable if the transmittance in these regions is notably lower than in regions with in-plane nerve fibres. When comparing the transmittance image (Fig. 3a) with the inclination image (Fig. 6a) for the coronal vervet brain section, it becomes apparent that cingulum and fornix fulfill this criterion (i. e. their transmittance is notably lower than the transmittance of the corpus callosum which contains mostly in-plane nerve fibres). The corona radiata is dotted with regions that show substantially darker transmittance values than the corpus callosum (caused by the superior longitudinal fascicle – a steep fibre tract crossing this region), but it also contains regions with similar transmittance values, indicating that the high inclination values in these areas cannot be considered as reliable and are most probably caused by in-plane crossing nerve fibres. As the threshold parameters in the transmittance histogram are very susceptible to small changes, we decided to keep an automated detection of crossing nerve fibres for future algorithms.

So far, the nerve fibre inclinations were computed by applying a transmittance-weighted model to the whole brain section and manually adjusting the parameters. The models presented here (with and without transmittance weighting in HM- and LM-regions, equations 1 and 2) lead to a major enhancement of the computed fibre inclinations in the grey matter (cf. Fig. 4(ii) and (iii)). The computation of an HM-probability map allowed for the first time to consider transition zones, reducing step artefacts at the boundaries between HM- and LM-regions (cf. Fig. 4(III) and (IV)): The course of nerve fibres from deep white matter regions into the cortex becomes much more continuous (yellow arrows), even border regions with sharp bending that were clearly visible as dark stripes become more softened (cyan arrows). However, the dark fissures of the inclination at the borders are still present in some regions and still need to be improved by another tuning of the  $m_{R+/-}$  and  $m_{T+/-}$  parameters. As shown in Fig. 6, the consistency of nerve fibre inclinations in whole coronal and sagittal brain sections of different species (monkeys and rodents) validates the reliability of the algorithms applied.

The findings presented in Fig. 5 show that the different models have different impacts on the computed inclinations of nerve fibre bundles (in the caudate putamen of a rat brain). When using the unweighted model (i), the computed inclinations are mostly independent of the real underlying fibre inclination. The transmittance-weighted model (ii) introduces the proportionality of the computed inclinations (they increase with increasing fibre inclination) in particular for values below  $50^\circ$ . The introduction of



the HM-probability map (iv), necessary to generate valid fibre inclinations in the grey matter and to obtain a smooth transition at the boundaries, has only a small impact on the computed fibre inclinations of the nerve fibre bundles: (iv) almost shows a similar behaviour as (ii). Hence, the linear combination of both models (equation 3) to compute the nerve fibre inclinations in regions with different degrees of myelination can be used without changing the inclination values in deep white matter structures. Although the transmittance-weighted inclinations (ii-iv) are much more realistic than those computed with the unweighted model (i), the comparison of 3D-PLI and two-photon fluorescence microscopy (TPFM) shows a strong over-estimation of the computed fibre inclinations ( $\Delta\alpha \approx 30^\circ$ ). However, the inclinations obtained from 3D-PLI might also be larger than those obtained from TPFM because the TPFM measurements have been performed several weeks afterwards so that the thickness of the brain section might have decreased due to dehydration. For this reason, a direct comparison of 3D-PLI and TPFM values is critical. However, as the affine image registration of 3D-PLI to TPFM measurements did not reveal large tissue deformations, maintaining also a high affinity of the corresponding direction angles, major deviations of the fibre orientations are unlikely.

In conclusion, we have introduced a versatile software that allows for the first time to automatically compute the out-of-plane angles of nerve fibres obtained from standard 3D-PLI measurements of brain tissue (without tilting). So far, these nerve fibre inclinations were computed by applying a transmittance-weighted model to the whole brain section, requiring anatomical knowledge and effortful manual adjustment of parameters. By distinguishing areas with different degrees of myelination and defining transition zones, we were able to apply a regionally specific computation of fibre inclinations that goes beyond the separation of white and grey matter and accounts for subtle changes in the tissue composition. The developed algorithm is parallelised and uses GPU acceleration, thus allowing for a fast and reproducible computation of nerve fibre inclinations for large brain sections and greatly improving the analysis and interpretation of 3D-PLI data also for past measurements.

## Methods

**Preparation of brain sections.** The brain sections were obtained from three healthy rats (Wistar, male, three months old) and two healthy vervet monkeys (male, between one and two years old). All animal procedures were approved by the institutional animal welfare committee at Forschungszentrum Jülich GmbH, Germany, and were in accordance with the European Union and National Institutes of Health guidelines for the use and care of laboratory animals. The monkey brains were obtained in accordance with the Wake Forest Institutional Animal Care and Use Committee (IACUC #A11-219). Euthanasia procedures conformed to the AVMA Guidelines for the Euthanasia of Animals. The brains were removed from the skull within 24 hours after death, fixed with 4 % buffered formaldehyde for several weeks, cryo-protected with 20 % glycerine and 2 % dimethyl sulfoxide, deeply frozen, and coronally or sagittally cut with a cryostat microtome (Polycut CM 3500, Leica, Microsystems, Germany) into sections of 60  $\mu\text{m}$ . A coronal vervet brain section (no. 512), a sagittal vervet brain section (no. 374), a coronal rat brain section (no. 185), and a sagittal rat brain section (no. 176) were selected for evaluation. The sections were mounted on glass slides, embedded in 20 % glycerine solution, cover-slipped, sealed with lacquer, and measured with 3D-PLI afterwards.

**3D-PLI measurements.** The 3D-PLI measurements were performed with the polarising microscope (LMP-1, Taorad GmbH, Germany), as described in Menzel *et al.*<sup>4,10</sup>: Incoherent light with a wavelength of about 550 nm was transmitted through a linear polariser, the brain section, and a circular analyser. The polariser was rotated in steps of  $10^\circ$  and for each rotation angle ( $\rho = \{0^\circ, 10^\circ, \dots, 170^\circ\}$ ) an image was recorded with a CCD camera (Qimaging Retiga 4000R), yielding a pixel size in object space of about 1.33  $\mu\text{m}$ . For each image pixel, the intensity values of the resulting image series form a sinusoidal signal with respect to the rotation angle, which can be described as:

$$I(\rho) = \frac{I_T}{2} \left( 1 + \sin \delta \sin (2(\rho - \varphi)) \right). \quad (4)$$

The average of the signal (*transmittance*  $I_T$ ) is a measure of the tissue attenuation, caused by absorption and scattering. The phase of the signal (*direction*  $\varphi$ ) indicates the in-plane direction angle of the nerve fibres. The amplitude of the normalised signal (*retardation*  $r = |\sin \delta|$ ) indicates the strength of birefringence and is related to the out-of-plane angle (*inclination angle*  $\alpha$ ) of the nerve fibres.

**Derivation of fibre inclination angle.** The retardation  $r$  is related to the inclination angle  $\alpha$  of the nerve fibres via<sup>5</sup>:

$$r = |\sin \delta| \approx \left| \sin \left( \frac{2\pi}{\lambda} \Delta n d_m \cos^2 \alpha \right) \right|, \quad (5)$$

where  $\lambda$  is the wavelength of the incident light,  $d_m$  the thickness of the birefringent tissue (myelin), and  $\Delta n$  the birefringence of the material, which are usually not precisely known<sup>1</sup>.

There exist several ways to compute the inclination angle, by making different assumptions:



- (a) **Unweighted model:** Assuming that  $\Delta n d_m$  does not change much within the measured brain section, the fibre inclination angle can be computed for each image pixel via:

$$\alpha = \arccos \left( \sqrt{\frac{\arcsin(r)}{\arcsin(r_{\max})}} \right), \quad (6)$$

where  $r_{\max}$  is the maximum retardation value of all image pixels, expected to occur in regions with densely packed, parallel in-plane nerve fibres ( $r_{\max} = r_{\alpha=0^\circ}$ ). To not take any outliers into account, the accumulated histogram of the retardation image is fitted by a sigmoid function on the entries with the highest retardation as described by Axer *et al.*<sup>1</sup>

- (b) **Transmittance-weighted model:** Usually, the amount of nerve fibres (and thus the amount of birefringent material  $d_m$ ) changes notably within a brain section. When using model (a), this yields to an over-estimation of the fibre inclination angles in regions with a small amount of nerve fibres. To take the different amounts of nerve fibres and hence the different retardation values into account, the transmittance is used as a reference. Due to the high scattering coefficient of myelin, regions with many nerve fibres appear darker than regions with less nerve fibres. When light with intensity  $I_0$  is transmitted through a material with thickness  $d$  and attenuation coefficient  $\mu$ , the resulting light intensity is attenuated according to the Lambert-Beer law:

$$I_T = I_0 \exp(-\mu d) \quad \Leftrightarrow \quad \mu d = \ln \left( \frac{I_0}{I_T} \right). \quad (7)$$

In brain tissue, the light passes through birefringent tissue (myelin) with attenuation coefficient  $\mu_m$ , and non-birefringent tissue (e. g. cell bodies) with attenuation coefficient  $\mu_c$ . For now, we assume that both attenuation coefficients do not depend on the exact tissue composition or the fibre inclination. The maximum thickness of birefringent tissue in the brain section is defined as  $d_M$ , and the transmittance in this region as:  $I_M = \tilde{I}_0 \exp(-\mu_m d_M)$ , where  $\tilde{I}_0$  is the transmitted light intensity taking the non-birefringent layer with thickness  $(d - d_M)$  into account:  $\tilde{I}_0 = I_0 \exp(-\mu_c(d - d_M))$ . Equivalently, we define the transmittance in a region that is completely filled with non-birefringent tissue as:  $I_c = \tilde{I}_0 \exp(-\mu_c d_M)$ . The transmittance in any other brain region is then defined as:  $I_T = \tilde{I}_0 \exp(-\mu d_M) = \tilde{I}_0 \exp(-\mu_m d_m) \exp(-\mu_c d_c)$ , with  $d_M = d_m + d_c$  and  $d_m$  being the local thickness of birefringent tissue. With these definitions, we can write:

$$\mu d_M = \mu_m d_m + \mu_c d_c = \mu_m d_m + \mu_c (d_M - d_m) \quad (8)$$

$$\Leftrightarrow d_m \stackrel{(8)}{=} d_M \frac{\mu - \mu_c}{\mu_m - \mu_c} \stackrel{(7)}{=} d_M \frac{\ln(I_c/I_T)}{\ln(I_c/I_M)}. \quad (9)$$

Inserting this into equation 5, yields a modified formula for the fibre inclination angle<sup>8</sup>:

$$\alpha = \arccos \left( \sqrt{\frac{\arcsin(r)}{\arcsin(r_{\max})} \cdot \frac{\ln(I_c/I_M)}{\ln(I_c/I_T)}} \right), \quad (10)$$

where  $r_{\max} = |\sin(2\pi \Delta n d_M / \lambda)|$  is the retardation of a region with parallel in-plane nerve fibres with  $d_m = d_M$  and  $\alpha = 0^\circ$ .

**Binary classification of LM- and HM-regions.** LM-regions, HM-regions, and background were separated as described in Benning *et al.*<sup>12</sup>: Based on the histograms obtained from retardation and transmittance images, the parameters  $r_{\text{thres}}$ ,  $I_{\text{thres}}$ , and  $I_{\text{back}}$  were computed as described in the following paragraph (see also Fig. 1a). All regions with large birefringence/retardation values (in-plane fibres) as well as regions with similar or lower transmittance values than the region with maximum birefringence (in-plane crossing and out-of-plane nerve fibres) were identified as HM-regions:  $(r > r_{\text{thres}}) \vee (I_T < I_{\text{thres}})$ . Regions with low birefringence and larger transmittance values were identified as LM-regions:  $(r \leq r_{\text{thres}}) \wedge (I_{\text{thres}} \leq I_T \leq I_{\text{back}})$ . All other regions (with notably larger transmittance values,  $I_T > I_{\text{back}}$ ) were considered as background. To prevent the background from having any influence on the computed fibre inclinations, the retardation and transmittance of all background pixels were set to their minimum and maximum value, respectively, before analysing the corresponding histograms.

Before computing the transmittance histogram, the values were normalised to [0,1] and a circular median filter with 5 px radius was applied to the transmittance image. We selected a radius of 5 px (and not 10 px as in Benning *et al.*) because a larger radius leads to more clouding artefacts in the resulting inclination map, while a smaller radius leads to increased noise and makes non-relevant details like cells more visible (cf. Fig. 3b). As in Benning *et al.*<sup>12</sup>, the threshold parameters  $r_{\text{thres}}$  and  $I_{\text{back}}$  were computed as the points of maximum curvature behind and before the biggest peak in the retardation and transmittance



histogram, respectively. In contrast to Benning *et al.*<sup>12</sup> who used 128 bins, we decided to use histograms with 256 bins in order to increase accuracy. However, histograms with 256 bins might show several small peaks or a plateau (see red circle in Fig. 1a), which makes the determination of the threshold parameters difficult. To ensure that no outliers were chosen, we first considered a histogram with 64 bins (see inset in Fig. 1a) and computed the threshold parameters (points of maximum curvature) in a range corresponding to the full-width at half-maximum (FWHM) of the peaks, using larger ranges as Benning *et al.*<sup>12</sup> to account for thinner peaks:  $20 \times \text{FWHM}$  behind the retardation peak and  $10 \times \text{FWHM}$  before the transmittance peak. Then, we considered histograms with 128 bins and recomputed the threshold parameters in a range of bins close to the previous results  $[2 \cdot (\text{result} - 1), 2 \cdot (\text{result} + 1)]$ . The last step was repeated for histograms with 256 bins. In this way, the computed threshold parameters stay close to the previous results while being more accurate. The threshold parameter  $I_{\text{thres}}$  was computed as the point of maximum curvature between  $I_{\text{rmax}}$  and  $I_{\text{back}}$ , where  $I_{\text{rmax}}$  is the average transmittance of the region with maximum retardation value (0.009 % to 0.011 % of the image size).

**HM-probability map.** To compute the HM-probability map, the threshold parameters  $r_{\text{thres}}$  and  $I_{\text{thres}}$  were recomputed 200 times from slightly different retardation and transmittance histograms, generated by randomly drawing 25 % of the pixels in the retardation and transmittance images, respectively (pixels can be drawn several times). Subsequently, the positive and negative means of the 200 resulting threshold parameters were computed (indicating deviations to larger or lower values than the originally computed parameters), where  $m_{R+/-}$  refer to the positive/negative means of the  $r_{\text{thres}}$  values and  $m_{T+/-}$  to those of the  $I_{\text{thres}}$  values. The computed means determine the width of the transition zone between LM- and HM-regions, which is described by an error function to achieve a smooth transition from LM = 0 to HM = 1, cf. top image in Fig. 2c. Depending on where the transmittance and retardation values of an image pixel lie within the transition zone, different values (between 0 and 1) were assigned. The HM-probability map was computed using the following formula:

$$P_{\text{HM}} = -0.5 \cdot \text{erf} \left( \cos \left( \frac{3}{4} \pi - \arctan 2 \left( \frac{\Delta I_T}{\Delta r} \right) \right) \cdot \sqrt{(\Delta I_T)^2 + (\Delta r)^2} \right), \quad (11)$$

where:

$$\Delta r \equiv \begin{cases} \left| \frac{r - r_{\text{thres}}}{m_{R+}} \right|, & r - r_{\text{thres}} > 0 \\ \left| \frac{r - r_{\text{thres}}}{m_{R-}} \right|, & r - r_{\text{thres}} \leq 0 \end{cases} \quad (12)$$

$$\Delta I_T \equiv \begin{cases} \left| \frac{I_T - I_{\text{thres}}}{m_{T+}} \right|, & I_T - I_{\text{thres}} > 0 \\ \left| \frac{I_T - I_{\text{thres}}}{m_{T-}} \right|, & I_T - I_{\text{thres}} \leq 0 \end{cases} \quad (13)$$

**Computation of parameters.** To compute the fibre inclination angle (using equations 6 and 10), additional parameters are needed:  $\{r_{\text{max}}, I_{\text{M}}, I_{\text{C}}\} \in [0, 1]$ . Just as for the separation of HM- and LM-regions, a median filter with 5 px radius was applied to the transmittance image beforehand. To preserve the borders between HM- and LM-regions, the median filter was applied to HM- and LM-regions separately (ignoring background pixels).

To avoid the saturation of image pixels ( $\alpha = 0^\circ$  or  $90^\circ$ ), the maximum retardation was computed for HM- and LM-regions separately, yielding  $r_{\text{max,HM}}$  and  $r_{\text{max,LM}}$ . The highest retardation value in LM-regions is closely related to  $r_{\text{thres}}$ , which separates HM- and LM-regions in the retardation histogram. Hence,  $r_{\text{max,LM}}$  was computed similar to  $r_{\text{thres}}$ , as the point of maximum curvature in the retardation histogram, considering only image pixels in the LM-regions ( $P_{\text{HM}} < 0.05$ ). The parameter  $r_{\text{max,HM}}$  was calculated using the highest retardation value in the HM-regions ( $P_{\text{HM}} \geq 0.95$ ) as reference. With the union-find connected components algorithm by Oliveira *et al.*<sup>17</sup>, a region with comparable high retardation values was generated that consists of around 0.01 % of the HM-regions (0.009 % to 0.011 %). The average of the highest 10 % of selected pixels was used as  $r_{\text{max,HM}}$ . The average transmittance of all these selected pixels was used as  $I_{\text{M}}$ . The mode of the transmittance values in the LM-regions ( $P_{\text{HM}} < 0.05$ ) was used as  $I_{\text{C}}$ .

As out-of-plane nerve fibres have lower transmittance values than in-plane fibres due to an increased amount of scattering (see Menzel *et al.*<sup>10</sup>), all (median-filtered) transmittance values smaller than  $I_{\text{M}}$  (transmittance value in the region with maximum thickness of birefringent tissue) were set to this value, so that  $I_T \geq I_{\text{M}}$ .

**Computation of nerve fibre inclinations.** Depending on the value of the HM-probability map ( $P_{\text{HM}}$ ), the nerve fibre inclination was computed using either the transmittance-weighted model for HM-regions (equation 10), the unweighted model for LM-regions (equation 6), or a linear combination of both models for transition regions:

$$\alpha = P_{\text{HM}} \cdot \arccos \left( \sqrt{\frac{\arcsin(r)}{\arcsin(r_{\text{max,HM}})} \cdot \frac{\ln(I_{\text{C}}/I_{\text{M}})}{\ln(I_{\text{C}}/I_T)}} \right) + (1 - P_{\text{HM}}) \cdot \arccos \left( \sqrt{\frac{\arcsin(r)}{\arcsin(r_{\text{max}}^*)}} \right), \quad (14)$$



where

$$r_{\max}^* \equiv P_{\text{HM}} \cdot r_{\max, \text{HM}} + (1 - P_{\text{HM}}) \cdot r_{\max, \text{LM}}. \quad (15)$$

Hence, in the transition zone between HM-and LM-regions, the original formula was slightly altered: instead of using the highest retardation value of the whole image, a linearly interpolated value of the maximum retardation in HM-and LM-regions was used.

**Software.** The HM-probability map and the nerve fibre inclinations were computed with the specifically developed open-source software *PLImig*. For more information, the reader is referred to our GitHub page (<https://github.com/3d-pli/PLImig>). Note that the readme file uses a different notation, following Benning *et al.*<sup>12</sup> (white/grey matter instead of HM/LM-regions,  $I_{\text{lower/upper}}$  instead of  $I_{\text{thres/back}}$ ).

The software uses the (normalised) transmittance and retardation images from 3D-PLI measurements as input and computes the corresponding HM-probability and inclination images, as described above. Common image formats (TIFF, NIfTI, HDF5) are supported. The computation runs completely automatically and requires no additional parameters. For testing purposes and to study different scenarios (e. g. unweighted vs. transmittance-weighted model), the user can define specific parameters for different steps in the computation ( $I_{\text{back}}$ ,  $I_{\text{thres}}$ ,  $I_{\text{rmax}}$ ,  $r_{\text{thres}}$ ,  $I_{\text{M}}$ ,  $I_{\text{C}}$ ,  $r_{\max, \text{HM}}$ ,  $r_{\max, \text{LM}}$ ).

The program code is written in C++, executable on Windows and Linux systems, and requires an NVIDIA graphics card. Depending on the available graphics memory, the images are processed in a different number of chunks to avoid overflow. RAM should be at least five times the image size to be processed. For the coronal and sagittal rat brain sections (417 MB and 843 MB, when using 32-bit float values), 8 GB are sufficient. For the coronal vervet brain section (6 GB), 32 GB are needed. To process the sagittal vervet brain section (6.5 GB) or larger brain sections, high-end desktops or servers with more memory are required. The software uses CUDA for the GPU implementation, OpenCV as image container, and OpenMP (supporting multi-platform shared-memory multiprocessing programming). The determination of the histogram threshold parameters (initial separation of LM/HM-regions) and the computation of the fibre inclinations are completely implemented on the GPU, so that no speedup is expected when increasing the number of CPU cores. The generation of the HM-probability map (generation of slightly different histograms by bootstrapping) uses CPUs, so that the computing time can be reduced with increasing numbers of CPU cores (running multiple iterations in parallel on the GPU). The size of the graphics memory determines the number of parallel iterations: each iteration requires twice the image size used for bootstrapping (here: 25 % of the original image size). As only histograms are calculated in each iteration, this part is memory and bandwidth bound on the GPU side, and CPU bound in the time it takes to create the random image. With increasing number of CPU cores, the program will be more GPU bound.

To enable fast processing of large images, the HM-probability maps and fibre inclinations were computed on the supercomputer JURECA<sup>18</sup>. Using 512 GB RAM, one GPU (NVIDIA A100 40GB) and 128 CPU cores on one node, the computing time for the coronal vervet brain section ( $34\,669 \times 46\,341$  pixels) takes 15 min for the HM-probability map and 5 min for the rest.

**TPFM measurements and analysis.** The TPFM measurements were performed on a coronal rat brain section ( $6 \times 8$  tiles in the caudate putamen, cf. Fig. 5b) that had previously been measured with 3D-PLI. The TPFM measurements were performed as described in Menzel *et al.*<sup>10</sup> with a custom-made two-photon fluorescence microscope<sup>13–15</sup> consisting of a model-locked titanium-sapphire laser with a wavelength of 800 nm and a water-immersion  $25\times$  objective lens (LD LCI Plan-Apochromat 25x/0.8 Imm Corr DIC M27), achieving a resolution of  $0.244 \times 0.244 \times 1\,\mu\text{m}^3$ . The fluorescence signals were collected by two photomultiplier tubes, detecting red and green fluorescence, respectively. TPFM allows a full in-depth scan of the  $60\,\mu\text{m}$  thin brain section, yielding one image every  $z = 1\,\mu\text{m}$ . The axial displacement was realised with a closed-loop piezoelectric stage. A motorised xy-stage enabled tile-wise scanning of the sample. The sample was measured in tiles of  $250 \times 250\,\mu\text{m}^2$ , with an overlap of 10 %, and the resulting images were stitched together using the software *TeraStitcher*<sup>19</sup>. Due to the slightly different autofluorescence signal of different tissue components, the nerve fibre bundles can be manually traced across different slices of a TPFM image stack. To determine the inclination angle of a fibre bundle, the cross-sections of the fibre bundle were determined in the first and last slices of the image stack that still show the fibre bundle. The inclination angle  $\alpha$  was computed geometrically from the midpoint positions of the cross-sections, taking the number of images (z-depth) between the first and last slice into account (cf. Fig. 5c). 230 fibre bundles in the caudate putamen were selected for evaluation. Only well-separated fibre bundles with well-defined fibre inclination were chosen. To enable a comparison between the geometrically computed TPFM inclinations and the automatically computed 3D-PLI inclinations, the transmittance image of the 3D-PLI measurement was registered onto the maximum intensity projection of the TPFM image stack (cf. Fig. 5b) using affine transformations, and the individual fibre bundles were masked in the registered transmittance image. To avoid registration artefacts, the inverse transformation was applied to the resulting fibre mask, allowing to locate the fibre bundles in the original (non-registered) inclination image. The average 3D-PLI inclination was then plotted against the corresponding TPFM inclination for each fibre bundle, applying different formulas to compute the 3D-PLI inclination (cf. Fig. 5e). To ensure that the tissue had not deformed



between measurements, the maximum intensity projection of the TPFM image stack was compared to the transmittance image, ensuring that visible borders of nerve fibre bundles overlap.

**Code availability.** The software *PLImig* that was used to compute the HM-probability maps and the nerve fibre inclinations is publicly available on GitHub (<https://github.com/3d-pli/PLImig>). Data analysis was performed with the open-source software *Fiji* (<https://fiji.sc/Fiji>).

**Data availability.** All data supporting the findings of this study are included in the provided figures.

## References

1. Axer, M. *et al.* A novel approach to the human connectome: Ultra-high resolution mapping of fiber tracts in the brain. *NeuroImage* **54**, 1091–1101, DOI: [10.1016/j.neuroimage.2010.08.075](https://doi.org/10.1016/j.neuroimage.2010.08.075) (2011).
2. Axer, M. *et al.* High-resolution fiber tract reconstruction in the human brain by means of three-dimensional polarized light imaging. *Front. Neuroinformatics* **5**, 1–13, DOI: [10.3389/fninf.2011.00034](https://doi.org/10.3389/fninf.2011.00034) (2011).
3. Zilles, K. & Tillmann, B. N. *Anatomie* (Springer Medizin Verlag, Heidelberg, 2010).
4. Menzel, M. *et al.* Scattered Light Imaging: Resolving the substructure of nerve fiber crossings in whole brain sections with micrometer resolution. *NeuroImage* **233**, 117952, DOI: [10.1016/j.neuroimage.2021.117952](https://doi.org/10.1016/j.neuroimage.2021.117952) (2021).
5. Menzel, M. *et al.* A Jones matrix formalism for simulating three-dimensional polarized light imaging of brain tissue. *J. Royal Soc. Interface* **12**, 20150734, DOI: [10.1098/rsif.2015.0734](https://doi.org/10.1098/rsif.2015.0734) (2015).
6. Dohmen, M. *et al.* Understanding fiber mixture by simulation in 3D Polarized Light Imaging. *NeuroImage* **111**, 464–475, DOI: [10.1016/j.neuroimage.2015.02.020](https://doi.org/10.1016/j.neuroimage.2015.02.020) (2015).
7. Schmitz, D., Amunts, K., Lippert, T. & Axer, M. A least squares approach for the reconstruction of nerve fiber orientations from tilttable specimen experiments in 3D-PLI. In *2018 IEEE 15th International Symposium on Biomedical Imaging (ISBI 2018)*, 132–135, DOI: [10.1109/ISBI.2018.8363539](https://doi.org/10.1109/ISBI.2018.8363539) (Washington, DC, USA, 2018).
8. Reckfort, J. *New Approaches to the Interpretation of 3D-Polarized Light Imaging Signals for an Advanced Extraction of Fiber Orientation*. Ph.D. thesis, University of Wuppertal (2015).
9. Schwarzmaier, H.-J. *et al.* Optical properties of native and coagulated human brain structures. *SPIE* **2970**, 492–499, DOI: [10.1117/12.275082](https://doi.org/10.1117/12.275082) (1997).
10. Menzel, M. *et al.* Toward a high-resolution reconstruction of 3D nerve fiber architectures and crossings in the brain using light scattering measurements and finite-difference time-domain simulations. *Phys. Rev. X* **10**, 021002, DOI: [10.1103/PhysRevX.10.021002](https://doi.org/10.1103/PhysRevX.10.021002) (2020).
11. Schuenke, M., Schulte, E. & Schumacher, U. *THIEME Atlas of Anatomy - Head and Neuroanatomy* (Georg Thieme Verlag, Stuttgart, Germany, 2007).
12. Benning, K., Menzel, M., Reuter, J. & Axer, M. Independent Component Analysis for noise and artifact removal in Three-dimensional Polarized Light Imaging. In Amunts, K., Grandinetti, L., Lippert, T. & Petkov, N. (eds.) *Brain-Inspired Computing. BrainComp 2019. Lecture Notes in Computer Science*, vol. 12339 (Springer, 2021).
13. Silvestri, L., Allegra Mascaro, A. L., Costantini, I., Sacconi, L. & Pavone, F. S. Correlative two-photon and light sheet microscopy. *Methods* **66**, 268–272, DOI: [10.1016/j.ymeth.2013.06.013](https://doi.org/10.1016/j.ymeth.2013.06.013) (2014).
14. Costantini, I. *et al.* Polarized Light Imaging and Two-Photon Fluorescence Microscopy correlative approach for 3D reconstruction of the orientation of myelinated fibers. *Opt. Life Sci. Congr. OSA Tech. Dig. (online), paper BrW4B.5* DOI: [10.1364/BRAIN.2017.BrW4B.5](https://doi.org/10.1364/BRAIN.2017.BrW4B.5) (2017).
15. Costantini, I. *et al.* Autofluorescence enhancement for label-free imaging of myelinated fibers in mammalian brains. *Sci. Reports* **11**, DOI: [10.1038/s41598-021-86092-7](https://doi.org/10.1038/s41598-021-86092-7) (2021).
16. Dammers, J. *et al.* Signal enhancement in polarized light imaging by means of independent component analysis. *NeuroImage* **49**, 1241–1248, DOI: [10.1016/j.neuroimage.2009.08.059](https://doi.org/10.1016/j.neuroimage.2009.08.059) (2010).
17. Oliveira, V. & Lotufo, R. A study on connected components labeling algorithms using gpus. vol. 2010 (2010).
18. Jülich Supercomputing Centre. JURECA: General-purpose supercomputer at Jülich Supercomputing Centre. *J. large-scale research facilities* **2**, A62, DOI: [10.17815/jlsrf-2-121](https://doi.org/10.17815/jlsrf-2-121) (2016).
19. Bria, A. & Iannello, G. TeraStitcher - a tool for fast automatic 3D-stitching of teravoxel-sized microscopy images. *BMC Bioinforma.* **13**, 316, DOI: [10.1186/1471-2105-13-316](https://doi.org/10.1186/1471-2105-13-316) (2012).



## Acknowledgements

We thank the lab team of the INM-1 (Institute of Neuroscience and Medicine, Forschungszentrum Jülich GmbH, Germany) for preparing the brain sections, Philipp Schlömer for the generation of the transmittance and retardation images, the members of the Fibre Architecture group (INM-1) for assisting in the manual evaluation of the TPFM inclinations, and Karl Zilles and Roger Woods for collaboration in the vervet brain project (National Institutes of Health under Grant Agreements No. R01MH092311 and 5P40OD010965). This work was funded by the European Union's Horizon 2020 Framework Programme for Research and Innovation under the Specific Grant Agreement No. 945539 ("Human Brain Project" SGA3) and the Helmholtz Association portfolio theme '*Supercomputing and Modeling for the Human Brain*'. We gratefully acknowledge the computing time granted through JARA-HPC on the supercomputer *JURECA*<sup>18</sup> at Forschungszentrum Jülich (FZJ).

## Author contributions statement

M.M. designed and supervised the research. J.R. developed the software and analysis methods, and visualised the results. M.M., J.R., D.G. and M.A. contributed to the analysis of the data. M.M., J.R., D.G., M.A. and K.A. contributed to the interpretation of the data. I.C. performed the TPFM measurements. M.M. wrote the first version of the manuscript. D.G., J.R., M.A., and K.A. contributed to the manuscript.

**Competing interests:** The authors declare no competing interests.